

Machine intelligence supports the full chain of 2D dendrite synthesis

Wenqiang Huang^{1,2,3,†}, Susu Fang^{2,†,*}, Xuhang Gu^{3,†}, Shen'ao Xue^{1,2}, Huanhuan Xing², Junjie Jiang^{1,2}, Junying Zhang^{1,2}, Shen Zhou⁴, Zheng Luo², Jin Zhang³, Fangping Ouyang^{1,5,6*}, and Shanshan Wang^{2,3*}

¹School of Physics, Hunan Key Laboratory for Super-Microstructure and Ultrafast Process, and Hunan Key Laboratory of Nanophotonics and Devices, Central South University, Changsha 410083, China

²College of Aerospace Science and Engineering, National University of Defense Technology, Changsha 410000, China

³School of Advanced Materials, Guangdong Provincial Key Laboratory of Nano-Micro Materials Research, Peking University Shenzhen Graduate School, Shenzhen 518055, China

⁴College of Science, National University of Defense Technology, Changsha 410000, China

⁵School of Physics and Technology, and Xinjiang Key Laboratory of Solid-State Physics and Devices, Xinjiang University, Urumqi 830046, China

⁶State Key Laboratory of Powder Metallurgy, and Powder Metallurgy Research Institute, Central South University, Changsha 410083, China

[†]These authors contributed equally.

*Corresponding authors: S.F. (fangsusugfd@nudt.edu.cn); F.O. (oyfp@csu.edu.cn); S.W. (wangshanshan08@nudt.edu.cn)

Exemplified by the chemical vapor deposition growth of two-dimensional dendrites, which has potential applications in catalysis and presents a parameter-intensive, data-scarce and reaction process-complex model problem, we devise a machine intelligence-empowered framework for the full chain support of material synthesis, encompassing rapid process optimization, accurate customized synthesis, and comprehensive mechanism deciphering. First, active learning is integrated into the experimental workflow, identifying an optimal recipe for the growth of highly-branched, electrocatalytically-active ReSe₂ dendrites through 60 experiments (4 iterations), which account for less than 1.3% of the numerous possible parameter combinations. Then, a prediction accuracy-guided data augmentation strategy is developed combined with a tree-based machine learning (ML) algorithm, unveiling a non-linear correlation between 5 process variables and fractal dimension (D_F) of ReSe₂ dendrites with only 9 experiment additions, which guides the synthesis of various user-defined D_F . Finally, we construct a data-knowledge dual-driven mechanism model by integration of cross-scale characterizations, interpretable ML models, and domain knowledge in thermodynamics and kinetics, unraveling synergistic contributions of multiple process parameters to the product morphology. This work demonstrates the ML potential to transform the research paradigm and is adaptable to broader material synthesis.

Introduction

Dendrites, a prevalent microstructure in solidification, play significant roles in capacitors¹, rechargeable batteries²⁻⁴, and sensors⁵. Its two-dimensional (2D) counterparts are featured with a high ratio of surface atoms, exotic edge states, and superior mechanical flexibility, displaying unique prospects in catalysis^{6,7}, non-linear optics^{8,9}, and dielectric memristors¹⁰. Chemical vapor deposition (CVD), which has achieved great success in the structure-controlled synthesis of various 2D single crystals¹¹⁻¹⁶, homo/heterostructures¹⁷⁻²⁰, and superlattices²¹⁻²⁴, is regarded as the most promising approach for the large-scale, high-quality preparation of 2D dendrites^{25,26}. **However, the CVD approach involves numerous synthesis parameters** (e.g., growth temperature, precursor type/dosage, reaction time, and carrier gas), **which constitute a vast search space with complex growth mechanisms lying behind, making the traditional trial-and-error method, such as the one factor at one time (OFAT), suffer from low efficiency, high cost, and poor transferability.**

Fortunately, machine learning (ML), as a mathematical tool adept at solving high-dimensional problems, is transforming the research logic of materials science²⁷⁻³¹ and holds great promise in the full-chain support to synthesis, specifically in achieving three long-sought goals: **(i) Efficient process optimization.** The ML approaches can find the optimal process corresponding to a material's extreme properties in a huge parameter space with as few experiments as possible. **(ii) Customized synthesis on demand.** Complex functional relationships between multiple process/component variables and material properties can be fitted via ML methods, so that researchers can easily obtain the recipe for the desired property values. **(iii) Multifactorial mechanism deciphering.** The impact of multiple parameters on the product performance can be evaluated simultaneously and quantitatively via interpretable ML approaches (e.g., SHapley Additive exPlanations, correlation analysis), so that a panorama of growth mechanisms involving multifactor importance analysis and synergies between variables can be unveiled.

Increasing efforts have been devoted to ML-assisted material synthesis in recent years. Notable studies include constructing ML-guided frameworks, such as active learning loops, supervised-learning workflows and transformer-based language models, to design all-natural plastic substitutes with diversified user-desired properties³², to discover multi-metallic perovskite oxides and alloys with record catalytic activities³³⁻³⁵, to optimize the manufacturing process for device efficiency improvement of solar cells³⁶, and to customize nanomaterial synthesis with controllable morphology, density, and optical wavelengths³⁷⁻⁴¹, etc. However, several limitations remain in prior work. **First, there is a lack of research cases where machine intelligence is utilized to empower the material growth from process optimization to customized synthesis to mechanism deciphering, especially for small data**, which may weaken the academic community's perception of ML's capability in the full-chain support for material synthesis. **Second, in terms of mechanism unraveling, the results given by the ML models are sometimes difficult to fully integrate with the material characterizations and expert knowledge.** Most interpretations involve only single variables, with a dearth of quantitative analysis of multiple factors, hindering the establishment of a growth mechanism that is truly interpretable, understandable, and comprehensive from the dual perspective of human and machine intelligence.

In this work, we select the CVD growth of 2D ReSe₂ dendrites as a model problem, in which ReSe₂ belongs to the low-symmetry triclinic crystal system with a more complex growth behavior that has rarely been studied compared with its high-symmetry counterparts (e.g., graphene, MoS₂, etc.), thus providing a

superior platform to validate machine intelligence empowerment in the whole chain of material synthesis. **First, an active learning loop is designed to find the optimal recipe** (involving 5 process variables) for the synthesis of 2D dendrites with a high fractal dimension (D_F) of 1.71 using only one-week experiments. **Second, a nonlinear mapping between multiple growth parameters and dendritic morphology of 2D ReSe₂ is constructed** using a gradient boosting framework with a prediction accuracy-guided data augmentation strategy, yielding a predictive capability of $R^2=0.86$ across the entire design space with a small budget of < 70 experiments. **Finally, a multifactorial growth mechanism is established by jointly applying cross-scale microscopic/spectroscopic characterizations, domain knowledge, and interpretable ML approaches**, thus unraveling synergistic effects of the rhenium source temperature, concentration, and the substrate type on the 2D ReSe₂ dendrite growth, which aligns with both human cognition and machine intelligence conclusions.

Results

Overview of the ML framework

Our ML framework comprises three modules: process optimization, customized synthesis, and mechanism deciphering, demonstrating the full-chain support of machine intelligence in the CVD synthesis of 2D ReSe₂ dendrites.

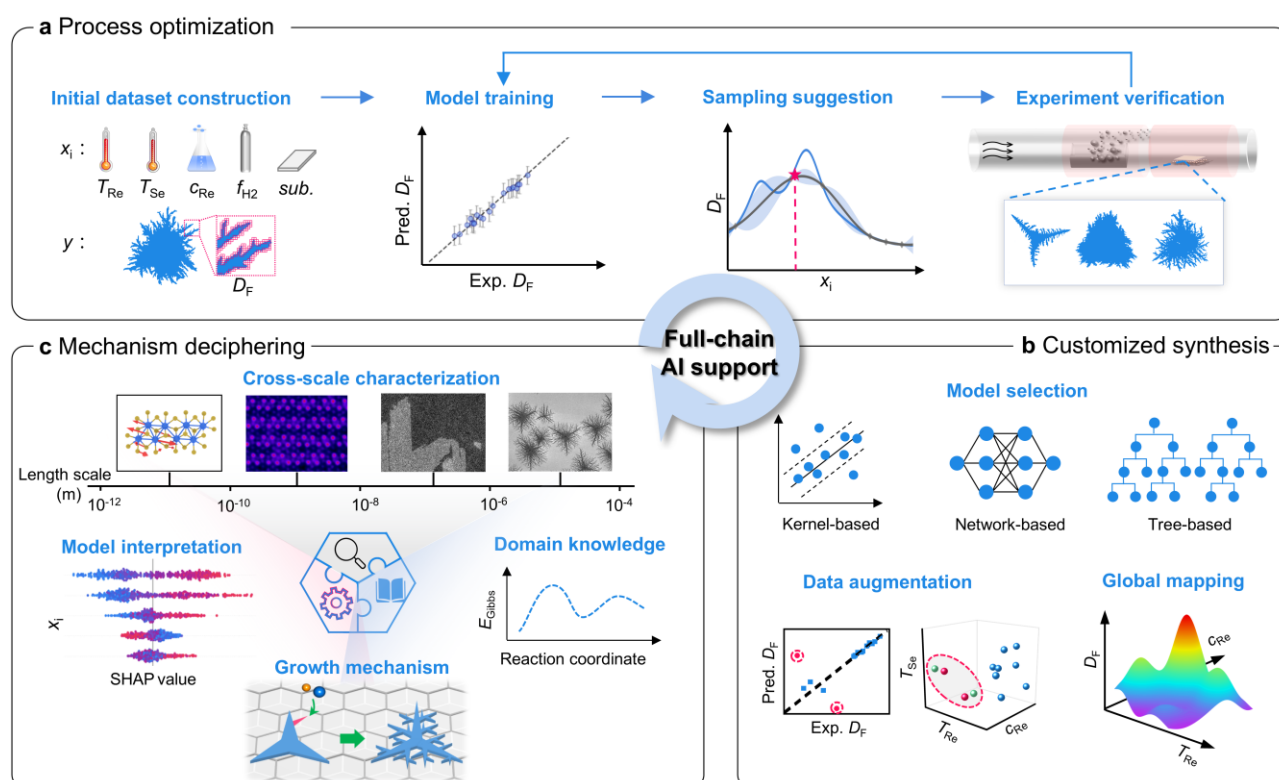


Fig.1 Scheme of the ML framework depicting the full-chain support of machine intelligence in the CVD preparation of 2D ReSe₂ dendrites. Three modules are included, i.e., (a) process optimization, (b) customized synthesis, and (c) mechanism deciphering.

Process optimization. This module is designed to quickly retrieve the optimal process conditions for the CVD growth of highly branched 2D ReSe₂ from a vast parameter space using as little experimental cost as possible (Fig. 1a). **First, the input variables (x_i) and the target output (y) for the active learning model are determined so that an initial dataset for iterative optimization can be established.** Five key process parameters are identified as x_i based on empirical knowledge, which are the heating temperature of

the rhenium source (T_{Re}), the heating temperature of the selenium powder (T_{Se}), the concentration of the rhenium source (c_{Re}), the flow rate of the hydrogen gas (f_{H_2}), and the substrate type (*sub.*). Their ranges are decided by a group of binary classification experiments (can grow *vs.* cannot grow) to ensure that the probability of growing 2D ReSe₂ within this sample space (involving 4752 condition possibilities) is high (Supplementary Tables 1-3). The fractal dimension (D_{F}), a metric quantifying geometric branching fineness, is introduced as y to evaluate the dendritic degree of ReSe₂ crystals, whose value can be programmatically extracted from scanning electron microscopy (SEM) images using a standard box-counting method (Supplementary Fig. 1). Twenty different process conditions are selected via Latin hypercube sampling (LHS) in order to generate a near-random sample of the input variable values from a multidimensional distribution (Supplementary Figs. 2 and 3). Their corresponding average D_{F} of the as-grown crystals are achieved by CVD experiments, preparing an initial dataset for the first round of model training. **Second, a Bayesian optimization (BO) strategy is utilized for active learning with Gaussian process regression (GPR) as the surrogate model.** This is mainly due to two reasons: i) there is a lack of any theoretical or empirical formulas to describe the explicit mathematical relationship between the CVD process variables and the crystal morphology, while BO-GPR excels at solving such a black-box function approximation problem; ii) BO-GPR is inherently capable of quantifying uncertainty over predictions. This nature allows a good balance between exploration and exploitation when sampling in new iterative cycles via acquisition functions, thus reaching a global optimum with a small experimental budget^{34,42,43}. **Third, Max-value entropy search (MES) is employed as the acquisition function to suggest new sampling points in the next round** after training the BO-GPR model with the initial dataset. This acquisition function leverages an information-theoretic perspective to maximize global information gain (accomplished by minimizing the information entropy of the objective function's maximum value) with minimum sampling cost⁴⁴. **Finally, CVD experiments corresponding to the process conditions suggested by MES are conducted to achieve new D_{F} which update the BO-GPR model iteratively** in the active learning loop until the improvement of D_{F} is close to saturation.

Customized synthesis. This module aims to construct a mapping between the five process variables and the dendritic morphology of ReSe₂, enabling easy determination of process conditions corresponding to various user-defined D_{F} (Fig. 1b). **Firstly, we select an ML model that is best suited to perform this regression task by comparing how well different models fit the data generated in Module 1.** Various models with distinct structures are considered, including kernel-based, network-based, instance-based, and tree-based ones. Notably, the optimization purpose of Module 1 leads to an uneven distribution of the accumulated data at this stage, which is skewed toward the high D_{F} regions. This deficiency results in a hardly satisfactory performance even for the best regression model, if solely using data achieved in Module 1 for training, since our target in Module 2 is to construct an accurate mapping between process variables and D_{F} across a wide value range. Therefore, **secondly, we develop a D_{F} prediction accuracy-guided data augmentation strategy.** Such discrepancy-based method supplements data for model tuning around the current data points with the poorest D_{F} prediction accuracy, which optimizes the worst-fitting regions with minimum addition of experiments. It is worth noting that we define a *PA* score, the square of the difference between the model-predicted and the experimental D_{F} values, to quantify the D_{F} prediction accuracy of every sampling point, which displays high sensitivity to data points with large prediction errors (see

equation (2) and more details in Fig. 3). After a few rounds of data augmentation and model optimization, a global mapping with satisfactory prediction performance can be attained.

Mechanism deciphering. This module is to unveil a multifactorial growth mechanism by integrating interpretable ML models, cross-scale spectroscopic/microscopic characterizations, and researchers' domain knowledge in thermodynamics and kinetics (Fig. 1c). We employ a feature-based interpretability method, called SHAP analysis, to quantify the importance of multiple process variables to D_F (SAHP values) and evaluate synergistic effects between features (SHAP interaction values)⁴⁵⁻⁴⁷. At the same time, a series of characterization techniques spanning from atomic to micrometer scales are performed, including Raman spectroscopy, annular dark-field scanning transmission electron microscopy (ADF-STEM), SEM, etc., to uncover morphology, orientations, and crystallinity of the as-grown 2D ReSe₂. Finally, the quantitative explanation from the ML algorithms and the qualitative understanding from material characterization and expertise are integrated to establish a data-knowledge dual-driven growth mechanism, which is comprehensive, precise, and understandable from both perspectives of human and machine intelligence.

Active learning-guided CVD process optimization

The active learning loop achieves prominent D_F improvement by a total of 60 experiments, which occupied <1.3% of the 4752 possible combinations in a grid search of the CVD parametric space. It begins with an initial dataset of 20 samples and undergoes 4 iterative cycles, each comprising 10 experiments. Fig. 2a is a box plot showcasing the progressive enhancement of D_F as the iterative cycle increases. We chose the median (hollow squares in the middle of boxes) to reflect the central tendency of D_F in each cycle, which is independent of data distribution and outliers compared with the mean. The D_F medians rise from 1.36 (iteration 0, initial dataset) to 1.61 (iteration 4), which attains a 69.4% boost in the feasible range ($D_F \in (1,2)$), see Methods, "Range of D_F ") and is intuitively manifested by increased roughness and intricate branches of the crystal edges via SEM images (top insets). In the final iteration, 2D ReSe₂ crystals with D_F up to 1.71 are obtained, exhibiting snowflake-like self-similar configurations with three-fold symmetry (inset, bottom right). Furthermore, the elevation rate of D_F with iterations exhibits a rapid jump at the early optimization stage, yielding a 47.2% enhancement in iteration 1, and gradually reaches saturation with a dramatic decay of the rising speed by more than an order of magnitude to <4% in iteration 4, which provides a clear decision-making indication for terminating the active learning loop. Interestingly, distinct from the monotonic increase of the D_F median, the distribution of D_F with iterations shows an "accordion"-style alternating expansion and contraction, as revealed by the widths of boxes in Fig. 2a. This suggests that the monotonic rise of D_F may be achieved through a trade-off between exploration (sampling in regions of high uncertainty to maximize information gain) and exploitation (sampling in regions with optimum predicted D_F to seek the largest objective reward) via the MES acquisition function during the iterative BO-GPR model training.

To uncover the optimization process, we drew 3D contour plots, which involve three key parameters (i.e., T_{Re} , c_{Re} , and T_{Se}) that contribute the most to D_F as the three coordinate axes (Supplementary Fig. 4) and the predicted D_F /uncertainty represented by the color of the contour map (Fig. 2b). When the BO-GPR model is trained using the initial 20 data points randomly selected by LHS, the temperature plane with $T_{Re} \approx 620^\circ\text{C}$ displays superior predicted D_F with low uncertainty. It leads the algorithm to concentrate all the sampling points on this T_{Re} plane in iteration 1 (exploitation strategy) but with a broad dispersion along the feasible range of T_{Se} in order to balance exploration (red dots and double-headed arrow in iteration 0 \rightarrow 1,

Supplementary Fig. 5). Since the algorithm adopts an exploitation strategy for the feature of T_{Re} , which has a dominant contribution to the model output, it brings about a fast increase of D_F with data distribution prominently narrowed compared with iteration 0 (magenta box in Fig. 2a). In iteration 2, the model chooses to scatter the sampling points in the c_{Re} dimension and prefers regions of higher uncertainty (red dots and double-headed arrow in iteration 1→2, Supplementary Fig. 6). Such an exploration-dominated strategy results in not only an obvious decrease in the D_F improvement rate but also an increase in the D_F dispersion compared to iteration 1 (green box in Fig. 2a). After a large-scale exploration of T_{Se} and c_{Re} in the first two iterations, sampling in iteration 3 focuses on a small range of $T_{Se} \approx 280^\circ\text{C}$ and $c_{Re} \approx 0.1 \text{ mol/L}$ with relatively high predicted D_F and uncertainty on the $T_{Re} \approx 620^\circ\text{C}$ plane (red circle in iteration 2→3, Supplementary Fig. 7). Such evolution of the sampling distribution from a large-range linear dispersion (iteration 2) to a small-range point-like concentration (iteration 3) leads to a drastically narrowed D_F distribution (yellow box in Fig. 2a). In the last iteration, the sampling points remain concentrated in a small region with a slight adjustment of T_{Se} and c_{Re} on the $T_{Re} \approx 620^\circ\text{C}$ plane in order to maximize the predicted D_F and minimize the uncertainty (red circle in iteration 3→4, Supplementary Fig. 8). This exploitation strategy leads to a minor enhancement of D_F but with a remarkable widening of data distribution compared to iteration 3 (gray box in Fig. 2a), which signifies that BO is approaching its limit.

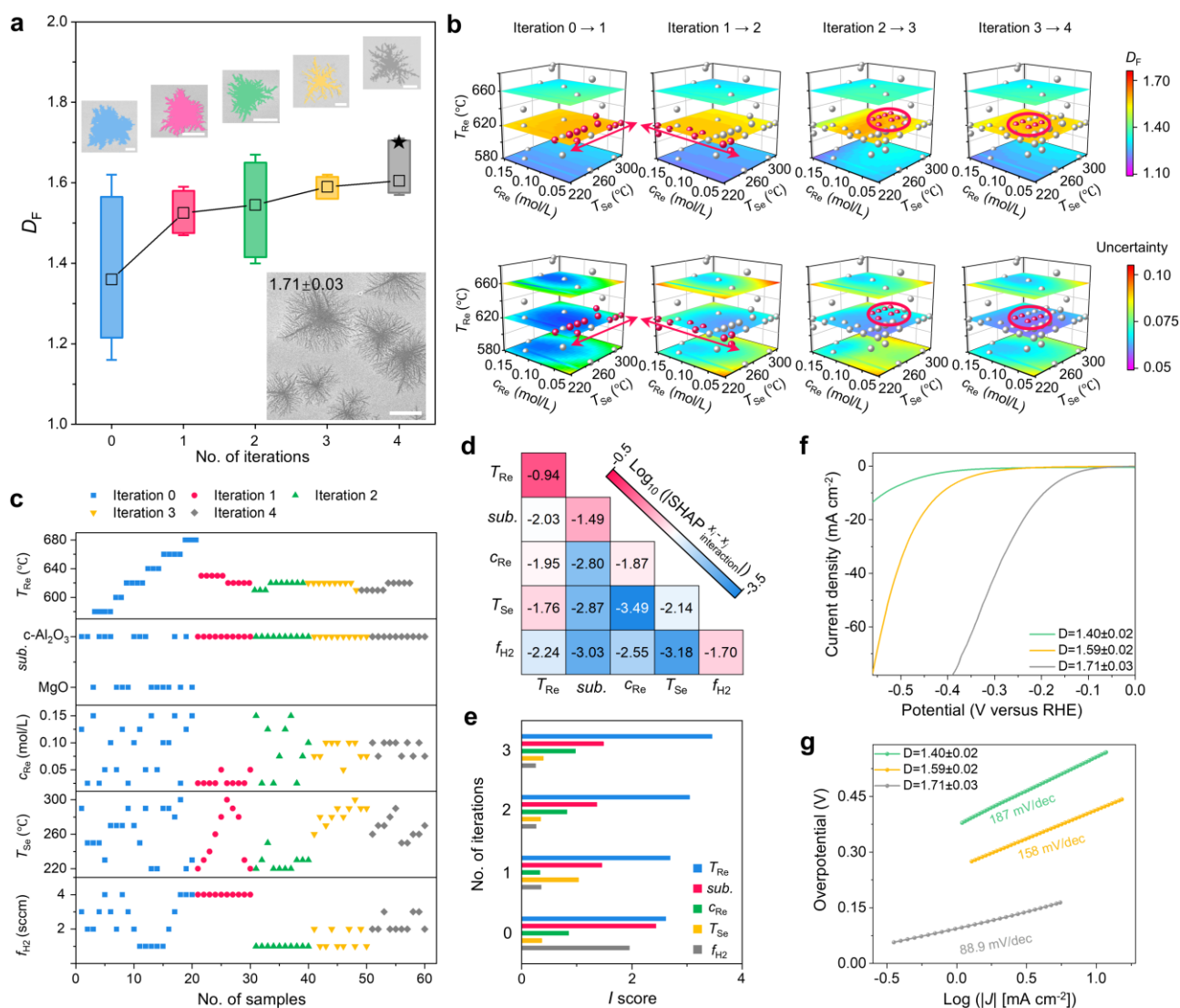


Fig. 2. Active learning-guided optimization of CVD process parameters for 2D ReSe₂ dendrites. **a**, Box plot showing the improvement of D_F with iterative cycles. Boxes: 10th-90th percentiles; whiskers: 3×interpercentile range;

hollow squares: medians. Insets (top) are false-color SEM images of 2D ReSe₂ dendrites corresponding to median D_F in iterations 0 to 4. Inset (right bottom) displays a typical SEM image of the ReSe₂ dendrites with a maximum $D_F = 1.71 \pm 0.03$ achieved in the final iteration (black star). **b**, Visualization of the BO process by exhibiting the three-dimensional CVD parameter- D_F plot and the sampling strategies in every iteration $s \rightarrow (s+1)$ ($s=0,1,2,3$). CVD parameters: T_{Re} , c_{Re} , and T_{Se} . Color bar (top panels): predicted average D_F . Color bar (bottom panels): uncertainty of the predicted D_F . The contour maps and gray dots represent the CVD parameter- D_F relation and the sampling points in iteration s , while the red dots represent the sampling points in iteration $(s+1)$. **c**, Evolution of five process parameters' values across four iterations. The initial dataset is called iteration 0 with a size of 20 experiments, represented by blue dots. 10 data points are appended in each new iteration, represented by magenta, green, yellow, and gray dots, respectively. **d**, SHAP interaction value matrix in the logarithmic form based on the BO-GPR model trained by the initial 20 data points in iteration 0. **e**, Histogram of I scores for the five CVD process parameters in 4 iterations. **f**, Cathodic linear sweep voltammetry (LSV) curves of ReSe₂ with D_F of 1.40 ± 0.02 , 1.59 ± 0.02 , and 1.71 ± 0.03 . **g**, The corresponding Tafel slopes.

The visualization of the active learning process reveals that the algorithm employs different sampling strategies (exploration vs. exploitation) for different input features. Such feature-dependent sampling behavior can be unveiled more clearly in Fig. 2c. Parameters of *sub.* and T_{Re} converge quickly to $c\text{-Al}_2\text{O}_3$ and $\approx 620^\circ\text{C}$, respectively, as soon as iteration 0 finishes, which corresponds to a continuous employment of the exploitation-based sampling on these two features throughout the BO process. c_{Re} experiences a large-scale sampling in the initial rounds, followed by a gradual convergence to ≈ 0.75 mol/L from iteration 3, indicating the application of an ‘‘exploration first, exploitation later’’ sampling strategy. Both T_{Se} and f_{H2} exhibit non-convergent behavior as their values change round by round even until iteration 4, implying the dominance of exploration-based sampling in these two variable dimensions. This feature-related convergence behavior suggests that the independence level of different features' impact on D_F varies. Process parameters that converge quickly mean that their values corresponding to the optimum D_F remain unchanged regardless of other parameters' values, whereas the variables that are difficult to converge imply that their values for the optimum D_F are heavily influenced by other features. We leveraged SHAP feature value analysis from collaborative game theory and proposed a measure, called I score, to quantify the independence level of each input variable's impact on the model output.

$$I \text{ score} = \frac{|\text{SHAP}_{\text{main effect}}^{x_i}|}{\sum_{i \neq j} |\text{SHAP}_{\text{interaction}}^{x_i-x_j}|} = \frac{|\text{SHAP}_{\text{interaction}}^{x_i-x_i}|}{\sum_{i \neq j} |\text{SHAP}_{\text{interaction}}^{x_i-x_j}|} \quad (1)$$

where $\text{SHAP}_{\text{main effect}}^{x_i}$ represents the SHAP main effect value of feature x_i , indicating the contribution of x_i to the model output when acting alone. It is equal to the SHAP interaction value of x_i with itself, denoted as $\text{SHAP}_{\text{interaction}}^{x_i-x_i}$. $\text{SHAP}_{\text{interaction}}^{x_i-x_j}$ represents the SHAP interaction value of two different features x_i and x_j , evaluating the synergistic contribution of x_i and x_j to the model output ($i \neq j$) (See Methods, ‘‘Quantification of the independence level of feature's impact on D_F ’’). The higher the I score is, the stronger the independence of this feature's impact on D_F becomes. The absolute values of SHAP interactions for the five CVD parameters after each iteration are displayed in logarithmically formed matrices (Fig. 2d and Supplementary Fig. 9) with the corresponding I scores calculated in Fig. 2e. The I scores of T_{Re} and *sub.* remain the top two highest among the five parameters in all iterations, which indicates their strong independence level of impact on D_F and is consistent with their fast convergence from iteration 1 in Fig. 2c. The I scores of c_{Re} are situated in the middle in most iterations, while those of T_{Se} and f_{H2} are at the bottom, in line with the moderate convergence rate of c_{Re} and non-convergence behaviors of T_{Se} and f_{H2} in active learning. It is noteworthy that the I score of f_{H2} reaches a relatively high value in iteration 0 with a

drastic decrease in the following three iterations, which coincides with the short-term stability of this feature's value in iteration 1 followed by three rounds of continuous fluctuations in BO.

Taking advantage of an abundance of nanoscale tips and unsaturated edge atoms, 2D ReSe₂ dendrites with high D_F are expected to exhibit superior hydrogen evolution reaction (HER) performance, which was evaluated using a three-electrode system in 0.5 M H₂SO₄ electrolyte (Supplementary Fig. 10). Cathodic linear sweep voltammetry (LSV) curves show that ReSe₂ with a D_F of 1.71 ± 0.03 exhibits an overpotential of only 195 mV at a current density of 10 mA cm⁻², representing a reduction of approximately 534 mV compared to ReSe₂ with a D_F of 1.40 ± 0.02 (Fig. 2f). Its Tafel slope is 88.9 mV dec⁻¹, indicating a Volmer-Heyrovsky mechanism with the Heyrovsky reaction as the rate-determining step^{48,49} (Fig. 2g and Supplementary Fig. 11). The increase in D_F promotes the rate-determining step to transform from the Volmer reaction ($\text{H}_3\text{O}^+ + \text{e}^- \rightarrow \text{H}_2\text{O} + \text{H}^*$) to the Heyrovsky reaction ($\text{H}_3\text{O}^+ + \text{e}^- \rightarrow \text{H}_2\text{O} + \text{H}_2$). The positive correlation between the HER performance of dendritic structures and their D_F not only verifies D_F as an effective descriptor to link morphological characteristics and catalytic properties but also suggests the efficacy of ML algorithms in optimizing material performance.

Process parameter- D_F model construction and interpretation

After finding an optimal parameter combination for the CVD synthesis of highly branched ReSe₂, we investigated the construction of an accurate relationship between the five process variables and D_F (Module 2). Six representative ML models, which can be categorized into instance-based (k-nearest neighbors (KNN) regressor), network-based (multilayer perceptron (MLP)), kernel-based (GPR and support vector regressor (SVR)), and tree-based (extra trees (ET) regressor and eXtreme Gradient Boosting (XGBoost) regressor) algorithms, are selected for training using the 60 data points accumulated in Module 1. The coefficient of determination (R^2) and mean square error (MSE), two metrics widely used to quantify the goodness of fit of a regression line to actual data, are employed to evaluate the model's performance (see Methods, "Model evaluation"). The best model should display both the maximal R^2 and the minimal MSE. Five repeated 5-fold cross-validations are conducted for each model to mitigate potential biases introduced by random data partitioning. Fig. 3a shows that two tree-based models outperform the other types of algorithms, where XGBoost wins the championship (Supplementary Fig. 12). It achieves an R^2 score of 0.74 and an MSE of 3.4×10^{-3} , which are 8.8% higher and 22.7% lower than those of the suboptimal model (i.e., ET).

However, due to the inhomogeneous distribution of data collected in Module 1, fitting for the process parameter- D_F curve is still not satisfactory across the entire feasible range of the parametric space, even utilizing the best XGBoost regressor. To improve the model predictive capability with minimal experiment addition, we develop a D_F prediction accuracy-guided data augmentation strategy, where a metric (called *PA* score), expressed as the square of the difference between the predicted and the experimental D_F values, is introduced to quantify the prediction error of each data point by the current model:

$$PA \text{ score} = \frac{1}{n} \sum_{i=1}^n \left(y_{\text{pred.}} - y_{\text{exp.}} \right)^2 \quad (2)$$

where $y_{\text{exp.}}$ and $y_{\text{pred.}}$ represent the experimentally measured and model-predicted D_F values, respectively. n represents the number of times the 5-fold cross-validation experiments are conducted. In this work, we performed 5 repeated 5-fold cross-validations for each data point to achieve its average prediction error (i.e., $n = 5$). To conduct data augmentation, we sorted the *PA* scores of all data points in Module 1 in descending order, chose the top three (red dots, left panel in Fig. 3b, Supplementary Table 4), and supplemented experiments in the vicinity of these three points in the process parameter space (green dots,

middle panel, Supplementary Table 5). This means the CVD process parameters of these new experiments are similar to those of the red dots, but not the same. Results of the supplemented experiments were incorporated into the original dataset for model retraining, which are expected to acquire significant improvement in the original worst-fit regions (right panel). After circulating this data augmentation process 3 times with only 9 experiments added in total (Supplementary Tables 6-9), R^2 and MSE of the XGBoost model are optimized step-by-step to 0.86 and 2.0×10^{-3} , which are 16.2% higher and 41.2% lower than before the data supplementation (Figs. 3c-e). In comparison, if 9 data points are added at once rather than divided into three iterative rounds, the model's MSE only decreases by 14.7% with an 8.1% enhancement of R^2 (Supplementary Table 10 and Supplementary Fig. 13). The global mapping of process parameter- D_F is displayed in Fig. 5 with a detailed analysis of the multifactorial growth mechanism.

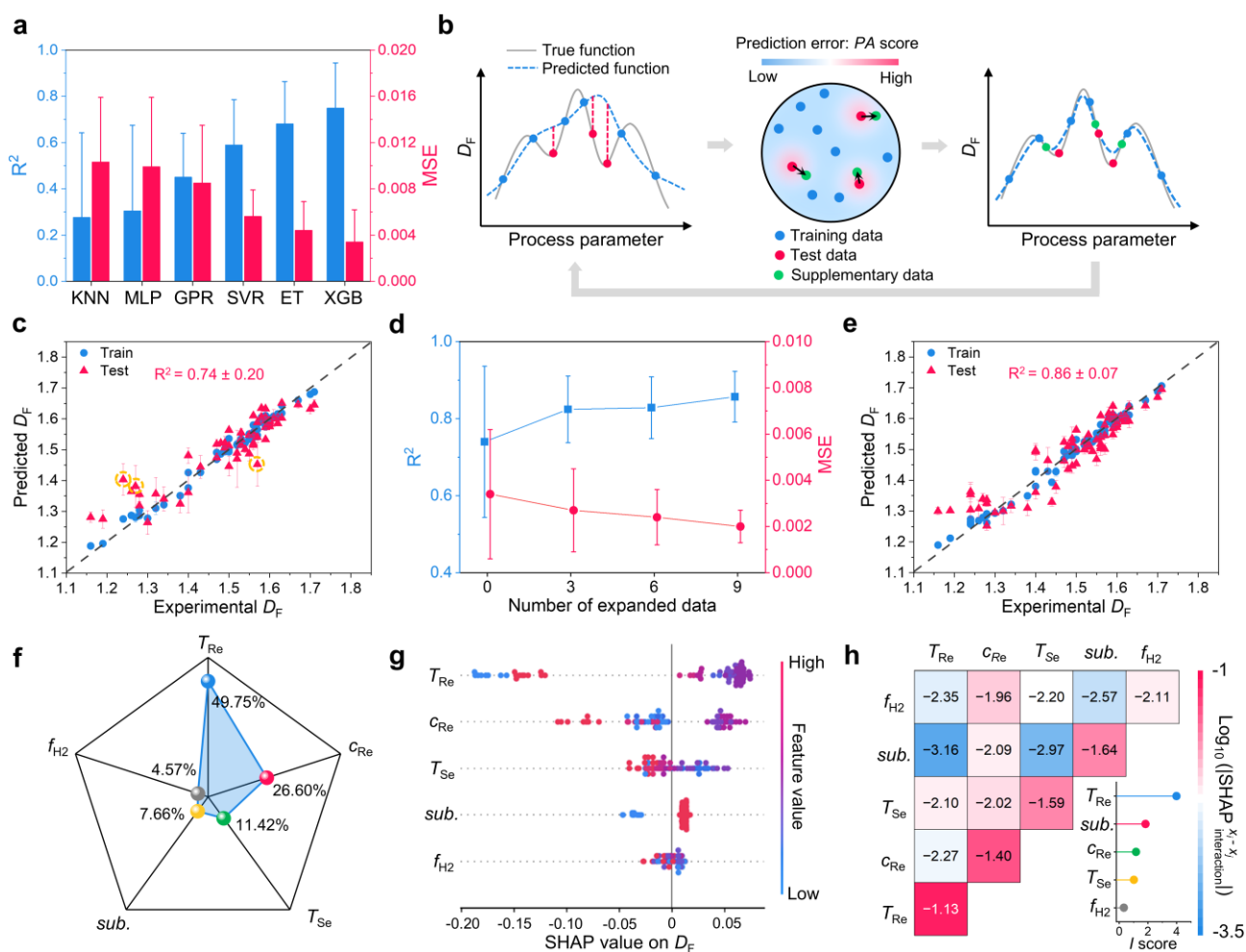


Fig. 3. Model construction and interpretation to reveal the process parameter- D_F relationship. **a**, Performances of the KNN, MLP, GPR, SVR, ET, and XGBoost models, evaluated by R^2 and MSE using the 60 data points collected in Module 1 for training. **b**, Schematic illustrating the principle of the D_F prediction accuracy-guided data augmentation strategy. **c**, Prediction performance of the XGBoost model before data augmentation. Yellow circles mark the three data points having the largest D_F prediction errors, which help locate the regions for data supplementation in the first iterative round. **d**, Evolution of R^2 and MSE values of the XGBoost model with the increase of the supplementary data points. **e**, Prediction performance of the XGBoost model after data augmentation with 9 experiments added. **f**, Feature importance of five CVD process parameters on D_F determined by normalized SHAP values. **g**, Beeswarm plot of SHAP values. **h**, SHAP interaction value matrix in the logarithmic form based on the XGBoost model after data augmentation. The inset is a histogram displaying the I scores of the five process parameters.

While the process parameter- D_F mapping regressed by the XGBoost model provides efficient guidance for the synthesis of 2D ReSe₂ with various user-defined D_F (Supplementary Fig. 14 and Supplementary

Table 11), the black-box nature of this ML model poses a challenge to understanding the internal rationale behind predictions. To improve the model's interpretability and uncover the process- D_F correlations for better mechanism deciphering (Module 3), we employed SHAP analysis, which can explain predictions of any ML model by calculating the importance of the input features and is versatile to provide both local explanations (per data point) and global feature importance. Fig. 3f shows that T_{Re} is the most influential process parameter to D_F , whose contribution accounts for nearly 50%. c_{Re} ranks second with a dramatic SHAP value decrease to 26.6%. The remaining three parameters, T_{Se} , $sub.$, and f_{H2} , account for less than a quarter of the overall contribution. This suggests that T_{Re} and c_{Re} play dominant roles in tailoring the morphology of 2D ReSe₂ dendrites and should be the focus of the domain knowledge-incorporated mechanism elucidation in the next section. It is worth noting that feature importance is not in alignment with the convergence behavior of different features in active learning. The input variable of $sub.$, which displays the fastest convergence rate in BO (Fig. 2c), has the second-lowest feature importance among the five parameters. This demonstrates the necessity of our proposed new metric, I score, which assesses the contribution independence of each feature to D_F , to explain the discrepancy in convergence behaviors of different features.

To get insights into the detailed impact of each feature on the model's output, we drew a beeswarm plot of the SHAP values (Fig. 3g), where five input features are arranged in a row and each dot represents a sample in the dataset with its color indicating the value of the feature. The horizontal position of each dot is determined by the SHAP value, indicating the magnitude and direction of a feature's impact on D_F . A positive value refers to a positive impact, and vice versa. Taking T_{Re} as an example, its widest distribution of SHAP values from -0.206 to $+0.079$ compared to the other inputs implies the strongest influence of this feature on D_F . Both high and low T_{Re} values make a negative contribution to D_F , while only intermediate ranges enhance D_F . Such a non-monotonic impact on the model's output is also observed in c_{Re} . In addition, the c -Al₂O₃ substrate (represented by a high feature value) demonstrates obvious D_F -promoting capability compared to MgO. Finally, the SHAP interaction matrix shows that the main effect of the features (i.e., the interaction effect of features with themselves) rather than the interaction effect between different features plays a dominant role to D_F , as manifested by larger values of the diagonal elements than non-diagonal elements (Fig. 3h). It indicates the absence of strong entanglement effects of these CVD process parameters on D_F . Besides, The I score ranking of the five features based on the XGBoost model after data augmentation is consistent with that obtained in active learning based on the GPR model, where T_{Re} and $sub.$ are the top two, verifying their strong independence level of impact on D_F regardless of the algorithm type and sample size.

Multiscale characterizations

Apart from extracting the apparent correlations between process parameters and D_F using interpretable ML algorithms, we also carried out multiscale microscopic and spectroscopic characterizations to unveil the morphology, orientation, and crystallinity of 2D ReSe₂ dendrites, which facilitates the proposal of a comprehensive and reliable growth mechanism (Module 3). Three key findings were discovered.

First, 2D ReSe₂ crystals evolve from isotropic circles to anisotropic dendrites as T_{Re} increases from 580 to 660°C (Fig. 4a). It is noteworthy that the fractal dimension of ReSe₂ grown at $T_{Re} = 620^\circ\text{C}$ ($D_F = 1.7$) is higher than that at $T_{Re} = 660^\circ\text{C}$ ($D_F = 1.5$), which is consistent with the results implied by SHAP

analysis (Fig. 3g) and further verifies the non-monotonic change of D_F with T_{Re} . **Second, ReSe₂ dendrites exhibit oriented growth strongly correlated with the substrate symmetry.** For ReSe₂ grown on *c*-Al₂O₃ with three-fold rotational symmetry (C_{3v}), two preferential orientations twisted by 60° are present, which is revealed by the angle concentration at 0° and 60° when measuring the smallest misorientation angle (α_1) between *c*-Al₂O₃[11 $\bar{2}$ 0] and the primary branches of ReSe₂ (Fig. 4b, top). Moreover, the minimum angles between the primary branches (α_2) and the minimum angles between the primary and secondary branches (α_3) are concentrated at 120° and 60°, respectively, showing orientation preference that corresponds to C_{3v} symmetry of *c*-Al₂O₃ (Fig. 4b, bottom). When the substrate changes to MgO(001), ReSe₂ dendrites are oriented along MgO[110] with the inter-branch angles (β_2 and β_3) concentrated at 90° (Fig. 4c, Supplementary Fig. 15), matching well with the four-fold rotational symmetry (C_{4v}) of this substrate surface. **Third, the CVD-grown 2D ReSe₂ dendrites are polycrystalline.** We measured the angle-dependent Raman intensities of the vibrational model at 162 cm⁻¹ in the parallel polarization configuration at different locations on one ReSe₂ crystal, where disordered patterns were achieved (Fig. 4d, blue and magenta lines), showing stark contrast to the well-oriented four-lobed patterns captured from an exfoliated single-crystalline sample (Fig. 4d, gray and brown lines). The ADF-STEM image shows that the edges of ReSe₂ dendrites are rugged, consisting of abundant ribbon-like structures that can be deflected by 60° (yellow markers, Fig. 4e, top), which demonstrates the edge roughness and the polycrystalline nature of ReSe₂ dendrites at the nanometer scale. When zooming in at a ribbon structure, well-organized Re₄ chains are observed with negligible defects at the atomic scale, indicating a high level of local crystal quality (Fig. 4e, bottom).

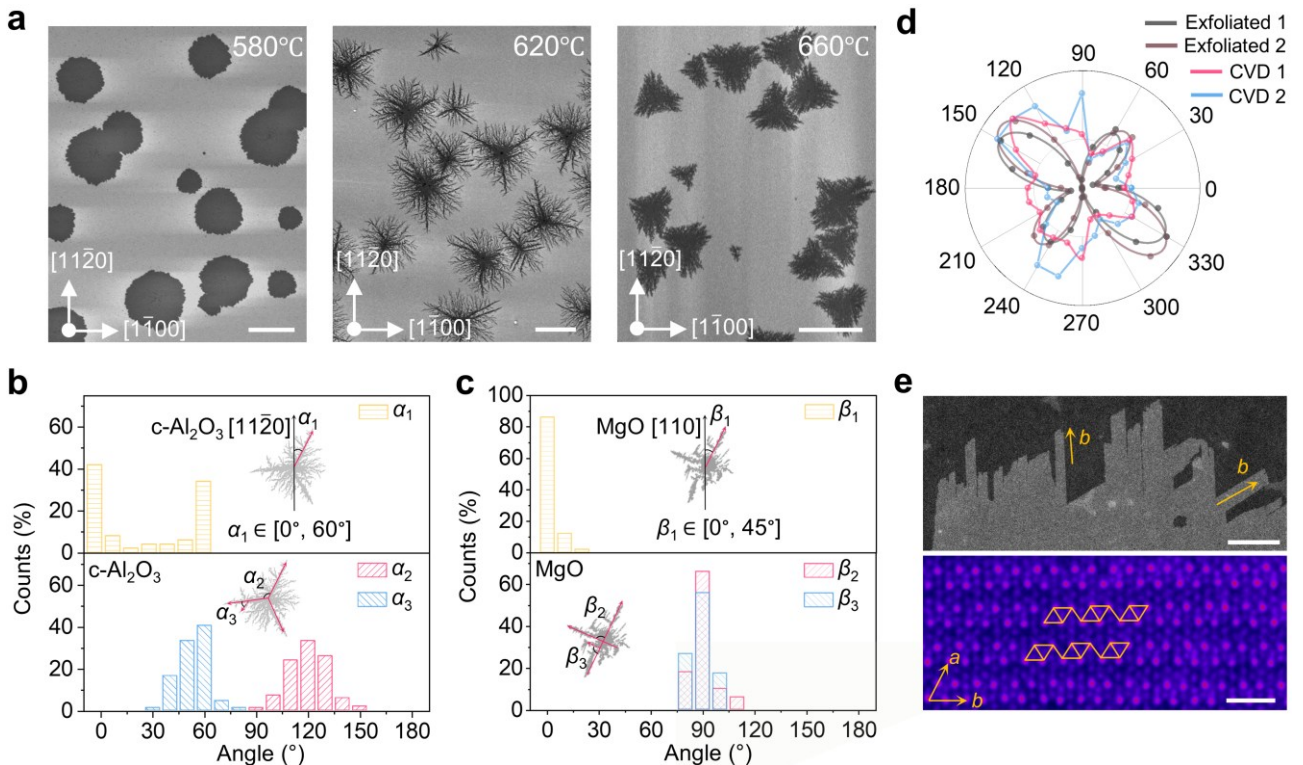


Fig. 4. Cross-scale characterizations of 2D ReSe₂ dendrites. **a**, SEM images showing the shape evolution of 2D ReSe₂ grown at T_{Re} =580, 620, and 660°C, respectively. The other CVD process parameters are fixed at $c_{Re} = 0.10$ mol/L, $sub. = c$ -Al₂O₃, $T_{se} = 250^\circ\text{C}$, $f_{H_2} = 2$ sccm. Scale bars (from left to right): 10 μm , 5 μm , 5 μm . **b**, Histogram showing the angle distribution of α_1 , α_2 , and α_3 of 2D ReSe₂ grown on *c*-Al₂O₃. α_1 : the minimum angle between *c*-Al₂O₃[11 $\bar{2}$ 0] and the primary branch of ReSe₂. α_2 : the minimum angle between the primary branches of ReSe₂. α_3 : the minimum angle between the primary and secondary branches of ReSe₂. Insets schematically illustrate α_1 , α_2 , and

α_3 . **c**, Histogram showing the angle distribution of β_1 , β_2 , and β_3 of 2D ReSe₂ grown on MgO(001). β_1 : the minimum angle between MgO[110] and the primary branch of ReSe₂. β_2 : the minimum angle between the primary branches of ReSe₂. β_3 : the minimum angle between the primary and secondary branches of ReSe₂. Insets schematically illustrate β_1 , β_2 , and β_3 . **d**, Angle-resolved Raman intensities of the vibrational model of ReSe₂ at 162 cm⁻¹ captured at two different locations on a CVD-grown ReSe₂ dendritic crystal (blue and magenta) and two different locations on a single-crystalline exfoliated ReSe₂ (gray and brown). **e**, Medium- and high-magnification ADF-STEM images of ReSe₂ dendrites. The yellow arrows indicate the *b*-axis of ReSe₂ (top), while the rhombus markers represent the Re₄ chains (bottom). Scale bars: 100 nm (top), 1 nm (bottom).

Multifactorial mechanism deciphering

We integrated quantitative information given by machine intelligence with qualitative understanding from material characterizations to establish a data–knowledge dual-driven growth model of 2D ReSe₂. Figure 5 (middle panel) displays a non-monotonic, non-linear correlation between the CVD process parameters and the ReSe₂ crystal morphology on the *c*-Al₂O₃ substrate, which is fitted by the XGBoost model using 69 sets of experimental data accumulated in Fig. 3. It involves the top two important features (T_{Re} and c_{Re}), identified by SHAP analysis, as the two *x*-coordinate axes, and D_{F} as the *y*-axis. **Combining results from ML and characterizations, key phenomena of 2D ReSe₂ grown on *c*-Al₂O₃ can be summarized:** (i) When T_{Re} is below 600°C, 2D ReSe₂ domains exhibit isotropic, circular, non-dendritic, polycrystalline structures; (ii) When T_{Re} rises above 600°C, 2D ReSe₂ polycrystals transform to anisotropic, dendritic morphology with branch orientations strongly correlated with the substrate symmetry; (iii) At $T_{\text{Re}} > 600^\circ\text{C}$, different combinations of T_{Re} and c_{Re} lead to a wide-range modulation of D_{F} from 1.4 to 1.7 (labels (i) to (iv) in Fig. 5, middle panel); (iv) T_{Re} has the strongest impact (~50%) on D_{F} followed by c_{Re} (~27%).

By incorporating domain knowledge, we proposed a multifactorial growth mechanism to explain these phenomena. **When T_{Re} is below 600°C, 2D ReSe₂ is thermodynamically controlled by an attachment-limited growth**, meaning that the adsorption and bonding of the precursor species to the domain edges is the rate-dominant step (Fig. 5, left panel). In this case, the surface energy of the system determines the preferential adsorption sites of the active species. Compared with crystal tips and edges, the attachment of precursor molecules to concavities reduces the surface energy the most. Therefore, any protrusions at domain edges will be quickly smoothed out under this mechanism, prohibiting the formation of dendritic structures thermodynamically. In addition, previous literature has reported that Re₄ chains are prone to deflect integer multiples of $\sim 60^\circ$ on *c*-Al₂O₃ during crystal growth due to the capability of forming highly coherent grain boundaries with low energy^{50,51}. This not only generates polycrystalline structures of ReSe₂ but also leads to a circular crystal shape due to isotropic growth rates in all lateral directions independent of either the substrate surface symmetry or the intrinsic crystal structure of the triclinic ReSe₂.

When T_{Re} exceeds 600°C, ReSe₂ swifts to kinetically controlled diffusion-limited growth (Fig. 5, right panel), where migration of precursor species on the substrate is the rate-dominant step. Our previous work has applied density functional theory calculations to unveil that the diffusion energy barrier of Re atoms on *c*-Al₂O₃ displays prominent anisotropy dependent on the lattice orientation of *c*-Al₂O₃⁵². Therefore, the macroscopic shape of polycrystalline dendrites and the preferential growth orientations of branches exhibit obvious association with the C_{3v} symmetry of *c*-Al₂O₃. It is noteworthy that, under diffusion-limited synthesis, the growth rate of 2D ReSe₂ at a certain temperature is affected by the concentration of precursor species absorbed on the substrate surface (commonly refers to Re concentration, because Se is in excess).

In our space-confined CVD setup constructed by two substrates placed face-to-face, Re precursor is spin-coated onto the lower substrate, which can be vaporized to adsorb onto the upper $c\text{-Al}_2\text{O}_3$ surface via heating for ReSe_2 dendrite growth (Supplementary Fig. 16). **Under this setup, the Re concentration adsorbed on the upper substrate surface is jointly influenced by T_{Re} and c_{Re}** , because T_{Re} dictates both the heating temperature of the bottom substrate coated with Re source and the temperature of the upper substrate at which adsorption equilibrium occurs, while c_{Re} impacts the supply amount of the Re source from the bottom substrate. Therefore, different combinations of T_{Re} and c_{Re} can vary D_{F} of dendrites.

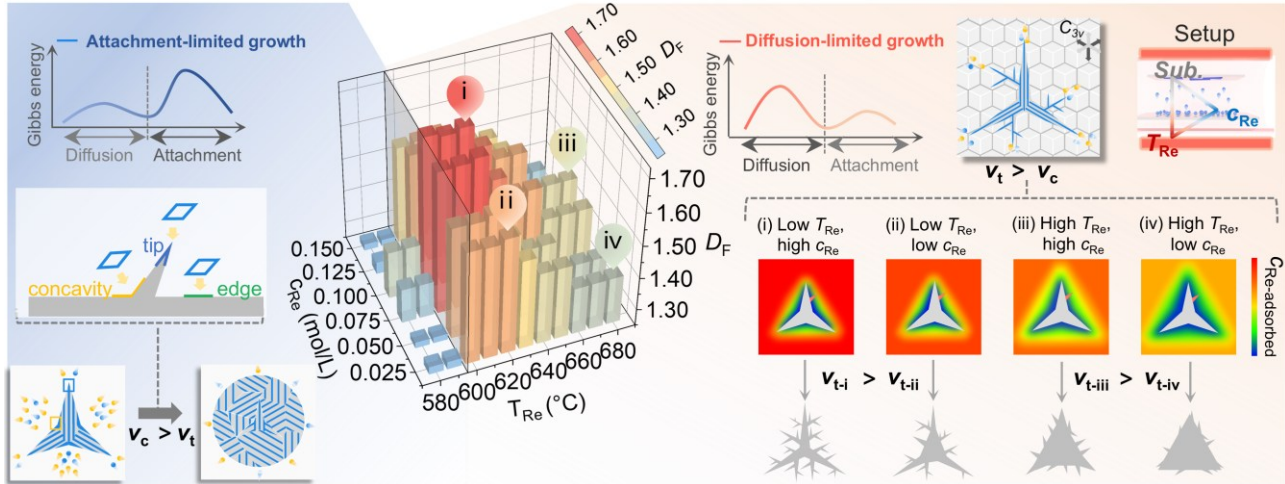


Fig. 5. Multifactorial growth mechanism deciphering of 2D ReSe_2 dendrites. Middle panel: Correlation between the most important CVD parameters (T_{Re} and c_{Re}) and D_{F} of 2D ReSe_2 crystals on $c\text{-Al}_2\text{O}_3$ fitted by the XGBoost model. Left panel: Attachment-limited growth when T_{Re} is below 600°C , where the formation of dendrites is thermodynamically prohibited due to a higher growth rate at the concavity region of the branch bottom (v_c) than at the branch tip (v_t). Right panel: Diffusion-limited growth when T_{Re} rises above 600°C , where a negative concentration gradient at the crystal edges results in a higher growth rate at the branch tip than at the branch bottom ($v_t > v_c$), allowing the formation of dendrites. v_{t-i} , v_{t-ii} , v_{t-iii} , and v_{t-iv} represent the growth rates of branch tips in cases (i) to (iv), respectively, which vary due to different combinations of T_{Re} and c_{Re} .

Take cases (i) and (ii) corresponding to low T_{Re} with high c_{Re} and low T_{Re} with low c_{Re} as an example to compare their products' D_{F} (Fig. 5, bottom right). Due to their same T_{Re} , the equilibrium Re adsorption concentration at the upper substrate surface (defined as c_{equ}) is solely determined by c_{Re} , thereby resulting in a higher c_{equ} of case (i) than that of case (ii). Furthermore, the heating temperature of the upper substrate, which equals T_{Re} , affects the migration ability of Re atoms on the substrate surface, thus determining the thickness of the depletion zone at the ReSe_2 crystal edge. The lower the T_{Re} temperature is, the narrower the depletion zone thickness becomes^{53,54}. Here, the depletion zone is the region with a negative concentration gradient of precursor species, extending from the edge of the ReSe_2 crystal to the location where the Re adsorption concentration reaches c_{equ} . When a branch is accidentally generated at the edge of a ReSe_2 domain due to energy perturbation and inserted into the depletion layer, the Re concentration at the tip of the branch is higher than at its base due to the presence of a negative concentration gradient within the depletion layer, which makes the branch not to be smoothed out and disappear, but rather to grow longer and longer. This explains why dendrites can be produced in diffusion-limited growth. Since case (i) has a higher c_{equ} than case (ii) and both cases adopt a low T_{Re} , a sharper negative Re concentration gradient is produced in the depletion layer under case (i) than under case (ii). Therefore, the branch tip under case (i)

is situated at a higher Re concentration than under case (ii), which gives ReSe₂ dendrites in case (i) a larger D_F . The D_F variations by other combinations of T_{Re} and c_{Re} can be demonstrated in a similar way.

Discussion

In this work, we display full-chain support of ML approaches to material growth under small datasets, including efficient recipe optimization, customized synthesis, and multifactorial mechanism deciphering, exemplified by the CVD growth of 2D ReSe₂ dendrites. First, the BO-GPR algorithm is performed, which improves D_F medians by 69.4% and achieves HER-active dendrites with a high D_F of 1.71 using 4 iterations (60 experiments), occupying less than 1.3% of the 4752 possible combinations in a grid search. Second, a prediction accuracy-guided data augmentation strategy is developed, which utilizes only 9 additional experiments combined with an XGBoost model to realize the establishment of a nonlinear mapping between 5 process variables and dendritic morphology of 2D ReSe₂. The model's predictive capability reaches $R^2=0.86$ across the entire feasible range and formulates data-informed guidelines to synthesize ReSe₂ dendrites with various user-defined D_F . Finally, we jointly apply cross-scale microscopic/spectroscopic characterizations, expert knowledge in thermodynamics and kinetics, and interpretable ML methods (SHAP feature analysis) to construct a data-knowledge dual-driven growth mechanism of 2D ReSe₂ dendrites, which unravels independent and synergistic contributions of multiple CVD parameters (T_{Re} , c_{Re} and *sub.*) to D_F . In addition, this work proposes two measures from the perspective of machine intelligence, namely I score and PA score. The former evaluates the independence of different features in contributing to the model output, so as to better understand the convergence behavior of input features during active learning process. The latter can guide the sampling strategy to improve the model's predictive capability with minimum experimental budget. Our approach can be generalized to the preparation of diversified materials and, more importantly, establishes a stylized ML-empowered framework for rapid material development and precise recipe-property relation establishment, which may revolutionize the research logic of material synthetic methodology.

Methods

Preparation and transfer of 2D ReSe₂

(i) Synthesis of 2D ReSe₂. The growth of 2D ReSe₂ was performed with a spatially confined CVD system^{16,18}. The spin-coated substrate served as the bottom chip, with another c-Al₂O₃ or MgO substrate placed face-to-face on top of it to form a space-confined reaction microchamber, which was positioned at the center of the high-temperature zone of the furnace (580-680°C). A 0.025-0.15 mol/L solution of ammonium perrhenate (NH₄ReO₄, 99%, RHAWN) was applied as a rhenium source and spin-coated onto the plasma-treated substrate surface at 5000 rpm for 30 seconds. The temperature of this substrate is the rhenium source temperature (T_{Re}). c-Al₂O₃ or MgO was treated with oxygen plasma to create a hydrophilic surface. For selenium (Se) source, 80 mg of Se powder (99.99%, RHAWN) was put in a ceramic boat at the center of the temperature zone of the furnace (220-300°C), and this temperature is defined as the T_{se} . Before 2D ReSe₂ synthesis, the CVD system was flushed with argon (Ar) gas flow for 10 min to remove the air from the tube. Subsequently, a mixed gas of Ar/H₂ was introduced, with Ar and H₂ gas flow rates (f_{H_2}) of 100 sccm and 1~4 sccm, respectively. The CVD system was maintained under the above-mentioned

conditions for 20 minutes to ensure the growth of ReSe₂ on the target substrate. After the growth period, the furnace was naturally cooled to room temperature under a continuous flow of Ar at ~500 sccm.

(ii) Transfer of 2D ReSe₂. A thin film of poly methyl methacrylate (PMMA) was spin-coated onto the ReSe₂/substrate surface. The coated substrates were baked at 80 °C for 3 minutes to strengthen the interaction between the PMMA film and the ReSe₂ and then floated on a 2 mol/L potassium hydroxide (KOH) solution to separate the PMMA/ReSe₂ film from the substrate. The detached PMMA/ReSe₂ film was transferred to deionized water three times to remove the residual etchants. Then, the film was transferred to a TEM grid or a glass carbon electrode, dried naturally in air, and baked on a hotplate at 100°C for 15 min. The sample was immersed in acetone for 8 h to remove the PMMA.

Characterizations

(i) Raman spectroscopy. Raman spectroscopy was employed to study structural properties, utilizing a Renishaw inVia confocal Raman system with an excitation wavelength of 532 nm. The laser power was kept below 100 μW, and the system was calibrated with the Raman peak of silicon at 520.7 cm⁻¹. The experimentally measured data of A_{1g}-like mode at 162 cm⁻¹ with parallel polarization $\bar{x}(yy)x$ or configurations are plotted as the blue and red dots, respectively. Under parallel polarization configuration, the angular dependence of the Raman intensity for this mode follows equations^{55,56}:

$$\begin{aligned}
 I_{A_g}^{\parallel} \propto & |a|^2 \cos^4 \theta + |d|^2 \sin^4 \theta + 4|b|^2 \sin^2 \theta \cos^2 \theta \\
 & + 2|a||d| \cos \phi_{ad} \sin^2 \theta \cos^2 \theta \\
 & + 4|a||b| \cos \phi_{ab} \sin \theta \cos^3 \theta \\
 & + 4|d||b| \cos \phi_{db} \sin^3 \theta \cos \theta
 \end{aligned} \tag{3}$$

Here, $I_{A_g}^{\parallel}$ is the Raman intensity for the A_g-like (162 cm⁻¹) mode in parallel polarization configurations. $|a|, |b|$ and $|d|$ are the value of Raman tensor element a, b , and d . θ is the angle between the incident laser polarization and the Re-chain direction (b-axis). $\phi_{ad} = \phi_a - \phi_d$, $\phi_{ab} = \phi_a - \phi_b$, and $\phi_{db} = \phi_d - \phi_b$.

(ii) ADF-STEM imaging. The measurements were conducted at room temperature on aberration-corrected Titan Cubed Themis G2 300. STEM was operated under an accelerating voltage of 300 kV. The experimental setup included a condenser lens with an aperture diameter of 50 μm. The convergence semi-angle was set to 21.3 mrad, and the collection angle ranged from 39 to 200 mrad. For each frame, the dwell time was set to 2 μs per pixel. Imaging was performed at a pixel size of 0.012 nm and a beam current of 30 pA.

Electrochemical measurements

HER measurements for 2D ReSe₂ with different D_F were performed at room temperature using a CHI 760E electrochemical workstation. The experimental setup consisted of a glassy carbon disk as the working electrode, a platinum plate as the counter electrode, and a saturated Ag/AgCl electrode as the reference, forming a standard three-electrode configuration. Linear sweep voltammetry (LSV) was conducted at a scan rate of 5 mV s⁻¹ in a 0.5 M H₂SO₄ electrolyte. Tafel slopes were obtained from the linear portions of the LSV curves using the Tafel equation, with current densities normalized based on the material's exposed surface area. Potentials were referenced to the reversible hydrogen electrode (RHE) using the relation E (vs RHE) = E (vs Ag/AgCl) + 0.197 V + 0.0592 pH.

ML models

(i) Bayesian optimization. BO operates by constructing a surrogate model to approximate the objective function and employs an acquisition function to guide subsequent experimental sampling, thereby identifying the global optimum with minimal experimental iterations. We set up the BO framework through the package Emukit in Python^{36,57}. The GPR model was selected as the surrogate model⁴³. GPR infers the distribution of the objective function across the parameter space using a limited number of data points and provides uncertainty estimates for predictions. Its mathematical formulation is as follows:

$$F(x) \sim N(\mu(x), K(x, x')) \quad (4)$$

where $\mu(x)$ is the mean function and $K(x, x')$ is the covariance function (kernel function).

The acquisition function recommends the experimental sampling points of the next iteration based on the surrogate model's predictions, balancing exploration (sampling regions with high uncertainty) and exploitation (regions predicted to yield near-optimal values). We employ the MES acquisition function, which selects sampling points by maximizing the information gain associated with the optimal value of the objective function⁴⁴. Its mathematical formulation is as follows:

$$\text{MES}(x) = H(p(f(x))) - E_{p(f(x^*))} [H(p(f(x)|f(x^*)))] \quad (5)$$

while $f(x)$ and $f(x^*)$ represent the predicted value and the predicted maximum value of the GPR, respectively. It is worth noting that all data were normalized prior to being fed into the model.

(ii) Model evaluation. Prior to feature analysis, ML models were evaluated using five repetitions of 5-repeated 5-fold cross-validation. Two indicators are selected to evaluate the model's performance, which are R^2 and MSE. R^2 is a statistical measure that provides information about the goodness of fit of a model. In the context of regression, it is a statistical measure of how well the regression line approximates the actual data. R^2 is $(-\infty, 1]$, where a value closer to 1 indicates better model performance. MSE measures the average squared difference between predicted and actual values, which disproportionately weights larger deviations, resulting in greater sensitivity to outlier values. R^2 and MSE were utilized to assess model performance, with their calculations shown as follows:

$$R^2 = 1 - \frac{\sum_{i=1}^n (y_{\text{pred.}} - y_{\text{exp.}})^2}{\sum_{i=1}^n (y_{\text{pred.}} - y_{\text{mean}})^2} \quad (6)$$

$$\text{MSE} = \frac{1}{n} \sum_{i=1}^n (y_{\text{pred.}} - y_{\text{exp.}})^2 \quad (7)$$

where $y_{\text{pred.}}$, $y_{\text{exp.}}$ and y_{mean} are the predicted D_F value, the experimental D_F value and the average of all the measured values, respectively.

(iii) XGBoost model. As an advanced implementation of gradient-boosted trees, XGBoost distinguishes itself through its efficient regularization techniques and parallel computing capabilities⁵⁸. Its core principle involves iteratively constructing multiple decision tree models and integrating them into a robust ensemble framework to enhance predictive accuracy. Its mathematical formulation can be expressed as:

$$y_{\text{pred.}} = \sum_{m=1}^M f_m(x_i) \quad (8)$$

where f_m denotes the base estimator, $y_{\text{pred.}}$ denotes the predicted D_F value, and x_i denotes the growth parameters value. $m=1, 2, \dots, M$.

The objective function comprises a loss function and a regularization term, mathematically expressed as:

$$\text{Obj}(\theta) = \sum_{i=1}^N L(y_{\text{pred.}}, y_{\text{exp.}}) + \sum_{m=1}^M \Omega(f_m) \quad (9)$$

where $L(y_{\text{pred.}}, y_{\text{exp.}})$ represents the MSE loss function, and $\sum_{m=1}^M \Omega(f_m)$ is the regularization term designed to control model complexity and mitigate overfitting. $i = 1, 2, \dots, N$.

Model interpretability

(i) Quantification of feature importance. We employed SHAP method to quantitatively assess the contribution of each input feature to predictions in the XGBoost model, thereby enhancing ML model's interpretability⁴⁶. Feature importance values are assigned by SHAP through calculating the marginal contributions of all possible feature subsets for each data instance. Global feature importance is derived by aggregating the mean absolute SHAP values across the entire dataset. SHAP also enables local interpretability by explaining predictions for individual instances through SHAP values. Features with larger mean absolute SHAP values exhibit higher importance and vice versa.

(ii) Quantification of the independence level of feature's impact on D_F . SHAP values can be decomposed into the independent effects of features (main effects, $\text{SHAP}_{\text{main effect}}^{x_i}$) and the mutual influences between features (interaction effects, $\text{SHAP}_{\text{interaction}}^{x_i-x_j}$, $i \neq j$). For any model prediction $f(x)$, SHAP guarantees the following additive decomposition:

$$f(x) = \phi_0 + \text{SHAP}_{\text{main effect}}^{x_i} + \text{SHAP}_{\text{interaction}}^{x_i-x_j} \quad (10)$$

where ϕ_0 is the baseline value, i.e., the model prediction when no features are considered. Therefore, using Equation (1), which is the ratio of the main effect to the interaction effect, to quantify the independence level of a feature's impact on D_F is reasonable and easy to understand.

Range of D_F . In this paper, we focus on the linear fractal dimension of dendrites, where $D_F \in (1, 2)$. Specifically, a value of 1 corresponds to a closed, smooth curve (exhibiting minimal geometric complexity). A value approaching 2 indicates a structure with non-zero area, which strictly speaking no longer qualifies as a "line" but instead approximates a plane. The D_F medians rose from 1.36 (iteration 0, initial dataset) to 1.61 (iteration 4). The improvement amount can be calculated using the normalization principle expressed as: $(1.61-1.36)/(1.36-1) \times 100\% = 69.4\%$.

Data availability

Relevant data supporting the key findings of this study are available within the article and the Supplementary Information file. All raw data generated during the current study are available from the corresponding authors upon request.

Code availability

All data supporting this study and the code are available on GitHub (<https://github.com/csuhwq0421/ML4Dendrites>).

References

1. Zhang, M. *et al.* Ultrahigh energy storage in high-entropy ceramic capacitors with polymorphic relaxor phase. *Science*. **384**, 185–189 (2024).

2. Li, L. *et al.* Self-heating–induced healing of lithium dendrites. *Science*. **359**, 1513–1516 (2018).
3. Ma, M. C., Li, G., Chen, X., Archer, L. A. & Wan, J. Suppression of dendrite growth by cross-flow in microfluidics. *Sci. Adv.* **7**, eabf694119 (2021).
4. Ning, Z. *et al.* Dendrite initiation and propagation in lithium metal solid-state batteries. *Nature* **618**, 287–293 (2023).
5. Xiao, B. *et al.* Preparation of hierarchical WO₃ dendrites and their applications in NO₂ sensing. *Ceram. Int.* **43**, 8183–8189 (2017).
6. Ji, Q. *et al.* Morphological engineering of CVD-grown transition metal dichalcogenides for efficient electrochemical hydrogen evolution. *Adv. Mater.* **28**, 6207–6212 (2016).
7. Shao, G. *et al.* Shape-engineered synthesis of atomically thin 1T-SnS₂ catalyzed by potassium halides. *ACS Nano* **13**, 8265–8274 (2019).
8. Chen, J. *et al.* Homoepitaxial growth of large-scale highly organized transition metal dichalcogenide patterns. *Adv. Mater.* **30**, 1704674 (2018).
9. Wang, B. *et al.* Fractal growth of 2D NbSe₂ for broadband nonlinear optical limiting. *Adv. Funct. Mater.* **34**, 2401490 (2024).
10. Kang, Y. *et al.* Conductive dendrite engineering of single-crystalline two-dimensional dielectric memristors. *Innovation* **6**, 100885 (2025).
11. Wang, M. *et al.* Single-crystal, large-area, fold-free monolayer graphene. *Nature* **596**, 519–524 (2021).
12. Liu, L. *et al.* Uniform nucleation and epitaxy of bilayer molybdenum disulfide on sapphire. *Nature* **605**, 69–75 (2022).
13. Wang, L. *et al.* Bevel-edge epitaxy of ferroelectric rhombohedral boron nitride single crystal. *Nature* **629**, 74–79 (2024).
14. Moon, D. *et al.* Hypotaxy of wafer-scale single-crystal transition metal dichalcogenides. *Nature* **638**, 957–964 (2025).
15. Wang, J. *et al.* Dual-coupling-guided epitaxial growth of wafer-scale single-crystal WS₂ monolayer on vicinal a-plane sapphire. *Nat. Nanotechnol.* **17**, 33–38 (2022).
16. Jiang, J. *et al.* Chirality-transferred epitaxy of circular polarization-sensitive ReS₂ monolayer single crystals. *Nat. Commun.* **16**, 7119 (2025).
17. Wang, S. *et al.* Atomic-scale studies of overlapping grain boundaries between parallel and quasi-parallel grains in low-symmetry monolayer ReS₂. *Matter* **3**, 2108–2123 (2020).
18. Chen, Y. *et al.* Constructing slip stacking diversity in van der waals homobilayers. *Adv. Mater.* **36**, 2404734 (2024).
19. Sahoo, P. K., Memaran, S., Xin, Y., Balicas, L. & Gutiérrez, H. R. One-pot growth of two-dimensional lateral heterostructures via sequential edge-epitaxy. *Nature* **553**, 63–67 (2018).
20. Li, W. *et al.* Robust growth of 2D transition metal dichalcogenide vertical heterostructures via ammonium-assisted CVD strategy. *Adv. Mater.* **36**, 2408367 (2024).
21. Xie, S. *et al.* Coherent, atomically thin transition-metal dichalcogenide superlattices with engineered strain. *Science*. **359**, 1131–1136 (2018).
22. Zhao, Y. *et al.* Supertwisted spirals of layered materials enabled by growth on non-Euclidean surfaces. *Science*. **370**, 442–445 (2020).
23. Xu, M. *et al.* Reconfiguring nucleation for CVD growth of twisted bilayer MoS₂ with a wide range of twist angles. *Nat. Commun.* **15**, 562 (2024).
24. Fortin-Deschênes, M., Watanabe, K., Taniguchi, T. & Xia, F. Van der Waals epitaxy of tunable moirés enabled by alloying. *Nat. Mater.* **23**, 339–346 (2024).
25. Zhang, Y. *et al.* Monolayer MoS₂ dendrites on a symmetry-disparate SrTiO₃ (001) substrate: formation mechanism and interface interaction. *Adv. Funct. Mater.* **26**, 3299–3305 (2016).

26. Li, J. *et al.* Fractal-theory-based control of the shape and quality of CVD-grown 2D materials. *Adv. Mater.* **31**, 1902431 (2019).
27. Dan, J. *et al.* Learning motifs and their hierarchies in atomic resolution microscopy. *Sci. Adv.* **8**, eabk1005 (2022).
28. Zhao, Q. *et al.* A machine learning–based framework for mapping hydrogen at the atomic scale. *Proc. Natl. Acad. Sci.* **121**, e2410968121 (2024).
29. Huang, W. *et al.* Auto-resolving the atomic structure at van der Waals interfaces using a generative model. *Nat. Commun.* **16**, 2927 (2025).
30. Luo, Z. *et al.* Exploring structure diversity in atomic resolution microscopy with graph. *Adv. Mater.* **37**, 2417478 (2025).
31. Crozier, P. A. *et al.* Visualizing nanoparticle surface dynamics and instabilities enabled by deep denoising. *Science.* **387**, 949–954 (2025).
32. Chen, T. *et al.* Machine intelligence-accelerated discovery of all-natural plastic substitutes. *Nat. Nanotechnol.* **19**, 782–791 (2024).
33. Moon, J. *et al.* Active learning guides discovery of a champion four-metal perovskite oxide for oxygen evolution electrocatalysis. *Nat. Mater.* **23**, 108–115 (2024).
34. Suvarna, M. *et al.* Active learning streamlines development of high performance catalysts for higher alcohol synthesis. *Nat. Commun.* **15**, 5844 (2024).
35. Kim, M. *et al.* Searching for an optimal multi-metallic alloy catalyst by active learning combined with experiments. *Adv. Mater.* **34**, 2108900 (2022).
36. Liu, Z. *et al.* Machine learning with knowledge constraints for process optimization of open-air perovskite solar cell manufacturing. *Joule* **6**, 834–849 (2022).
37. Lin, X. *et al.* Machine learning-assisted dual-atom sites design with interpretable descriptors unifying electrocatalytic reactions. *Nat. Commun.* **15**, 8169 (2024).
38. Tang, B. *et al.* Machine learning-guided synthesis of advanced inorganic materials. *Mater. Today* **41**, 72–80 (2020).
39. Zhang, J. *et al.* Toward controlled synthesis of 2D crystals by CVD: learning from the real-time crystal morphology evolutions. *Nano Lett.* **24**, 2465–2472 (2024).
40. Guo, H. *et al.* Machine learning-guided realization of full-color high-quantum-yield carbon quantum dots. *Nat. Commun.* **15**, 4843 (2024).
41. Li, Y. *et al.* Transforming the synthesis of carbon nanotubes with machine learning models and automation. *Matter* **8**, 101913 (2025).
42. Shields, B. J. *et al.* Bayesian reaction optimization as a tool for chemical synthesis. *Nature* **590**, 89–96 (2021).
43. Seeger, M. Gaussian processes for machine learning. *Int. J. Neural Syst.* **14**, 69–106 (2004).
44. Wang, Z. & Jegelka, S. Max-value entropy search for efficient Bayesian optimization. In *Proc. of the 34th International Conference on Machine Learning*, **7**, 5530–5543 (2017).
45. Lundberg, S. M. & Lee, S. I. A unified approach to interpreting model predictions. In *Proc. of the 31st International Conference on Neural Information Processing Systems*, 4766–4775 (2017).
46. Lundberg, S. M. *et al.* From local explanations to global understanding with explainable AI for trees. *Nat. Mach. Intell.* **2**, 56–67 (2020).
47. Muschalik, M. *et al.* shapiq: shapley interactions for machine learning. In *Proc. of the 38th International Conference on Neural Information Processing Systems*. **4141**, 130324–130357 (2024).
48. Xie, J. *et al.* Controllable disorder engineering in oxygen-incorporated MoS₂ ultrathin nanosheets for efficient hydrogen evolution. *J. Am. Chem. Soc.* **135**, 17881–17888 (2013).
49. Wang, X. *et al.* Single-atom vacancy defect to trigger high-efficiency hydrogen evolution of MoS₂. *J. Am. Chem. Soc.* **142**, 4298–4308 (2020).

50. Li, X. *et al.* Nanoassembly growth model for subdomain and grain boundary formation in 1T' layered ReS₂. *Adv. Funct. Mater.* **29**, 1906385 (2019).
51. Chen, X. *et al.* Diverse spin-polarized in-gap states at grain boundaries of rhenium dichalcogenides induced by unsaturated Re-Re bonding. *ACS Mater. Lett.* **3**, 1513–1520 (2021).
52. Hu, P. *et al.* Lateral and vertical morphology engineering of low-symmetry, weakly-coupled 2D ReS₂. *Adv. Funct. Mater.* **33**, 2210502 (2023).
53. Xu, J., Srolovitz, D. J. & Ho, D. The adatom concentration profile: a paradigm for understanding two-dimensional MoS₂ morphological evolution in chemical vapor deposition growth. *ACS Nano* **15**, 6839–6848 (2021).
54. Zhuang, J. *et al.* Morphology evolution of graphene during chemical vapor deposition growth: a phase-field theory simulation. *J. Phys. Chem. C* **123**, 9902–9908 (2019).
55. Choi, Y. *et al.* Complete determination of the crystallographic orientation of ReX₂ (X = S, Se) by polarized Raman spectroscopy. *Nanoscale Horizons* **5**, 308–315 (2020).
56. Zhao, H. *et al.* Interlayer interactions in anisotropic atomically thin rhenium diselenide. *Nano Res.* **8**, 3651–3661 (2015).
57. Paleyes, A., Mahsereci, M. & Lawrence, W. Emukit: A Python toolkit for decision making under uncertainty. In *Proc. of the 22nd Python in Science Conference*. 68-75 (2023)
58. Chen, T. & Guestrin, C. XGBoost: A scalable tree boosting system. In *Proc. of the 22nd ACM SIGKDD International Conference on Knowledge Discovery and Data Mining*. 785–794 (2016).

Acknowledgments

S.W. acknowledges support from the National Natural Science Foundation of China (52222201, 52172032, 22494464013), Major Fundamental Research Project of Hunan Province (2025JC0005), Shenzhen Science and Technology Innovation Commission Project (KQTD20221101115627004), and National University of Defense Technology (ZZCX-ZZGC-01-07). F.O. acknowledges support from the Key Project of the Natural Science Program of Xinjiang Uygur Autonomous Region (Grant No. 2023D01D03) and the computing resources at the High Performance Computing Center of Central South University.

Author contributions

S.W. initiated the project and generated experimental protocols. W.H. wrote the code. S.W. prepared the STEM samples and captured images. X.G. grew 2D crystals. S.X. and S.F. prepared the samples and conducted measurements. H.X., J.J., S.Z., Z.L., J.Z. and Y. O. discussed the work and gave suggestions. All authors contributed to the data analysis, manuscript writing, and revision of the manuscript.

Conflict of interest

The authors declare no competing interests.